


Can Polarity-Inverted Surfactants Self-Assemble in Nonpolar Solvents?

Manuel Carrer, Tatjana Škrbić, Sigbjørn Løland Bore, Giuseppe Milano, Michele Cascella, and Achille Giacometti*

 Cite This: *J. Phys. Chem. B* 2020, 124, 6448–6458

 Read Online

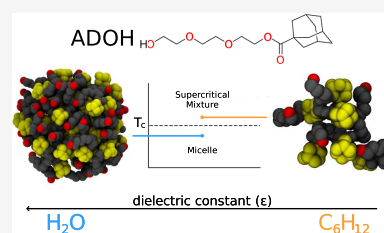
ACCESS |

 Metrics & More

 Article Recommendations

 Supporting Information

ABSTRACT: We investigate the self-assembly process of a surfactant with inverted polarity in water and cyclohexane using both all-atom and coarse-grained hybrid particle-field molecular dynamics simulations. Unlike conventional surfactants, the molecule under study, proposed in a recent experiment, is formed by a rigid and compact hydrophobic adamantane moiety, and a long and floppy triethylene glycol tail. In water, we report the formation of stable inverted micelles with the adamantane heads grouping together into a hydrophobic core and the tails forming hydrogen bonds with water. By contrast, microsecond simulations do not provide evidence of stable micelle formation in cyclohexane. Validating the computational results by comparison with experimental diffusion constant and small-angle X-ray scattering intensity, we show that at laboratory thermodynamic conditions the mixture resides in the supercritical region of the phase diagram, where aggregated and free surfactant states coexist in solution. Our simulations also provide indications as to how to escape this region to produce thermodynamically stable micellar aggregates.



1. INTRODUCTION

Life as we know it could not exist without water. In fact, living cells survive in environments mainly constituted by water. Cellular shape and functionality are determined by the presence of both the plasma and the cytoplasmic membrane, which define all of the necessary compartments for the organization of cellular matter and prevent the mixing of the cell with its external environment. To this aim, living organisms typically exploit biological lipids, amphiphile molecules comprising a strongly polar head group and one or more long hydrocarbon tails.¹ In aqueous solutions, these amphiphilic molecules tend to aggregate driven by “like-to-like” interactions that are usually referred to as the hydrophobic effect.² Within this general framework, water is unique because it forms hydrogen bonds with itself as well as with the polar moiety of the amphiphilic molecule. Hydrogen bonds play a special intermediate role as they have a strength of the order of 10–40 kJ/mol (corresponding to 5–10 $k_B T$ /bond at 298 K), much stronger than van der Waals interactions (≈ 1 kJ/mol) and considerably weaker than ionic or covalent bonds (≈ 100 kJ/mol or more). Also, hydrogen bonds have an intermediate orientation-dependence that is in between the strongly directional covalent and isotropic van der Waals interactions.

While this marvelous balance is the result of millions of years of evolution, it is possible to imagine that a similar outcome could be achieved in different biological environments under different conditions, such as those present in other planets of our universe. Although water has been detected in various thermodynamic states in our solar system, an alternative

scenario suggests the possibility of using polarity-inverted membranes in nonpolar solvents, such as the hydrocarbons frequently found in earth-like systems (see the recent review by Sandström³). Motivated by this idea, a number of related studies have recently been conducted. Pace and collaborators investigated protein stability in a nonaqueous solvent such as cyclohexane (C_6H_{12}).⁴ Hayashi et al. found that while proteins have well-defined unique structures in water, this is generally not the case in other nonpolar solvents.^{5,6} The stabilities of single polar and hydrophobic amino acids in water and nonpolar solvents have also been studied (unpublished results). To close the triangle of life, the stability of B-DNA under nonaqueous conditions has also been recently assessed.⁷

Notwithstanding the large number of studies that have been addressing the issue, the basic mechanism underlying a solvophobic effect in nonpolar solvents is still far from being fully understood. In its simplest terms, it could be stated as follows. If the polarity of amphiphilic molecules is inverted, so to have a hydrophobic (rather than polar) head and a polar (rather than hydrophobic) tail, would they self-assemble in nonpolar solvents, for example, C_6H_{12} ? If so, what would the driving force be?

Received: May 29, 2020

Revised: July 2, 2020

Published: July 3, 2020



Recently such an experiment has been performed on a newly synthesized molecule having exactly these features.⁸ This molecule, henceforth referred to as ADOH, is formed by a rigid and compact adamantane moiety AD and a long and floppy tail that consists of a triethylene glycol (TEG) with a characteristic group $\text{O}-\text{CH}_2-\text{CH}_2$ capped at the end by a hydroxyl group that is able to form hydrogen bonds (Figure 1).

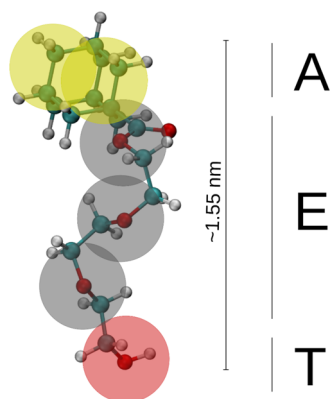


Figure 1. Molecular structure of ADOH. The transparent beads represent the coarse-grained mapping used for the hybrid particle-field molecular dynamics (hPF-MD) simulations. The labels identify the three different functional groups: A = adamantane, E = TEG, and T = OH.

The self-assembly properties of ADOH were studied by measuring its diffusion coefficient in C_6H_{12} , using NMR spectroscopy at different concentrations. A monotonic decrease of the diffusion coefficient, which is a possible signal of the micellization process, was observed in the concentration range from 5 to 250 mM and this hypothesis was further supported by small-angle X-ray scattering (SAXS) measurements that appeared to indicate a critical micelle concentration (CMC) around 100 mM. While through the Stokes–Einstein equation this decrease in the diffusion coefficient can be ascribed to the appearance of large aggregates, it alone does not constitute proof of the existence of aggregates with a well-defined micellar shape, especially considering the fact that directional-dependent polar interactions, such as hydrogen bonds, are significantly stronger compared with nondirectional van der Waals interactions. Moreover, while SAXS experiments provide essential system information on properties such as micelle sizes, the interpretation of aggregates in terms of shapes requires postprocessing by modeling, which is prone to errors. Thus, a molecular picture of aggregation is often hard to obtain.

Molecular modeling can complement experiments by providing molecular resolution predictions on the spatial organization of the molecules. In general, surfactant aggregation is a challenging process to simulate as it is facilitated by slow diffusing molecules and typically occurs at very low concentrations requiring both very large system sizes and long simulation times. For this specific ADOH surfactant system, the expected drop in diffusion coefficient occurs at very high concentrations, making it within reach of standard all-atom simulations. Nevertheless, all-atom simulations are computationally expensive and, even for this high-concentration regime, they may be affected by significant finite-size effects and may be limited in the range of accessible time scales.

Both of these drawbacks can be effectively addressed using coarse-grained modeling.^{9,10} In coarse-grained models, a lower resolution representation of the molecular structure with effective potentials is used to lower the overall computational cost, thereby allowing for the study of larger and longer simulations. For soft matter systems in particular, such as ADOH, the coarse-grained methodology of hybrid particle-field molecular dynamics (hPF-MD) has already been proved to be particularly effective. In hPF-MD, the coarse-grained molecular resolution description is combined with density-field modeling of intermolecular interactions to yield a computationally efficient modeling of very large systems. Applications of hPF-MD have started from more conventional soft polymer mixtures and then have moved also to biological systems.^{11–14} Examples from the literature include nanocomposites, nanoparticles, percolation phenomena in carbon nanotubes,^{15–18} lamellar and nonlamellar phases of phospholipids,^{19–22} and more recently polypeptides,²³ and polyelectrolytes.^{24–28} These applications, in particular polyelectrolytic molecules and surfactants (Triton X-100),²⁹ give us sufficient ingredients for building a hPF-MD model for ADOH.

Thus, the aim of the present work is to provide a molecular understanding of the nature of the putative ADOH aggregates reported in ref 8, as well as the underlying physical driving forces. Using both all-atom and hPF-MD numerical simulations, the self-assembly properties of ADOH molecules will be studied both in C_6H_{12} and in water under the same conditions reported in the experiment. While for the former case this will provide a complementary description with respect to the experiment, the latter case in water represents a new prediction that could eventually lead to further experimental testing.

The rest of the article is organized as follows. Section 2 outlines the all-atom and hPF-MD methods used in the present article. Section 3 reports the results, while Section 3.3 provides a connection to the experimental findings. Finally, Section 4 includes the key messages of the present study as well as some perspectives for future work.

2. METHODS

2.1. All-Atom Simulations. *NPT* all-atom simulations were run using the all-atom optimized potentials for liquid simulations (OPLS-AA) force field³⁰ with a time step of 2 fs. The temperature was set to 300 K and the pressure to 1 atm. The coupling was ensured by applying the *v*-rescale thermostat,³¹ with a relaxation time of 0.1 ps, and the Parrinello–Rahman barostat,³² with coupling constant set to 3 ps and isothermal compressibility equal to $4.5 \times 10^{-5} \text{ bar}^{-1}$. Long-range electrostatics was calculated with the PME method using a fourth-order interpolation, a 0.16 nm Fourier spacing, and a 1.2 nm cutoff, which was the same also for the calculation of short-range van der Waals interactions. Bond lengths were constrained using the LINCS algorithm.³³ The water model used was the TIP4P,³⁴ while for C_6H_{12} we used the parameterization implemented in the OPLS-AA force field.³⁵ The all-atom simulations were run with the GROMACS 2018.4 software.³⁶

2.2. hPF-MD Approach. In hPF-MD, molecular dynamics is used to sample the phase space of a fully resolved molecular system composed of N_{mol} molecules with Hamiltonian

$$\mathcal{H} = \sum_{n=1}^{N_{\text{mol}}} \mathcal{H}_0(\mathbf{r}_n) + \mathcal{W}[\phi(\mathbf{r})] \quad (1)$$

Here, $\mathcal{H}_0(\mathbf{r}_n)$ is the Hamiltonian of a single noninteracting molecule and $\mathcal{W}[\phi(\mathbf{r})]$ is the interaction energy that depends on the particle density ϕ .

To model nonbonded attraction and repulsion between particles, we employ the following interaction energy³⁷

$$\mathcal{W}[\phi(\mathbf{r})] = \frac{1}{2\phi_0} \int d\mathbf{r} \left[\sum_{ij} \tilde{\chi}_{ij} \phi_i(\mathbf{r}) \phi_j(\mathbf{r}) + \frac{1}{\kappa} \left(\sum_i \phi_i(\mathbf{r}) - \phi_0 \right)^2 \right] \quad (2)$$

where ϕ_0 is the total number density, $\tilde{\chi}_{ij}$ is the interaction term between species i and j , $\phi_i(\mathbf{r})$ and $\phi_j(\mathbf{r})$ are the number densities of the i th and j th species calculated at positions \mathbf{r} , and κ is a compressibility term. The net effect of \mathcal{W} is an external potential V_i acting on all particles of type i , which is obtained by

$$V_i(\mathbf{r}) = \frac{\delta \mathcal{W}[\phi(\mathbf{r})]}{\delta \phi_i(\mathbf{r})} = \frac{1}{\phi_0} \left[\sum_j \tilde{\chi}_{ij} \phi_j(\mathbf{r}) + \frac{1}{\kappa} \sum_j (\phi_j(\mathbf{r}) - \phi_0) \right] \quad (3)$$

The force acting on a particle of type i is obtained by gradient operation on V

$$\mathbf{F}_i(\mathbf{r}) = -\nabla V_i = -\frac{1}{\phi_0} \sum_j \left(\tilde{\chi}_{ij} + \frac{1}{\kappa} \right) \nabla \phi_j(\mathbf{r}) \quad (4)$$

Calculations of the potentials and of the forces acting on the particles, and those used to integrate the equations of motion, are computed with a particle mesh approach. For more details, we refer to ref 38.

2.3. hPF-MD Simulations. Figure 1 shows the CG mapping chosen for ADOH, while in Table 1 we report the bead interaction matrix $\tilde{\chi}_{ij}$ used in the present work. The $\tilde{\chi}$ values for C_6H_{12} and ADOH were selected from chemically similar moieties of Triton X-100 from ref 29.

Table 1. Interaction Matrix $\tilde{\chi}_{ij}/\text{kJ}\cdot\text{mol}^{-1}$ Used in the hPF-MD Simulations

	A	E	T	C (C_6H_{12})	W (H_2O)
A	0	7.8	13.25	0	33.75
E	7.8	0	4.5	7.8	1.5
T	13.25	4.5	0	13.25	0
C (C_6H_{12})	0	7.8	13.25	0	
W (H_2O)	33.75	1.5	0		0

CG simulations were run in the NVT ensemble using the OCCAM software.³⁸ The time step was set to 30 fs and the temperature was kept constant at 300 K by applying the Anderson thermostat³⁹ with a collision frequency of 7 ps⁻¹. The density field was updated every 20 time steps. In this model, each C_6H_{12} molecule is represented by a single bead, while a water bead comprises four molecules. For the

simulations in C_6H_{12} , we added small alternating partial charges (+0.4 and -0.4, chosen equal as the all-atom charges assigned to ether oxygens) on ADOH tail beads. This was done to qualitatively mimic the weak electrostatic interactions that, from atomistic simulations of the system with and without partial charges on the TEG segment, were found crucial in describing the clustering of the surfactant in the apolar solvent. The electrostatic potential in this case follows the Poisson equation with a relative dielectric constant $\epsilon_r = 5$ and its computation is performed using the recently developed adopted PME approach as in refs 24, 25. The composition of all simulated systems is reported in Table 2.

3. RESULTS AND DISCUSSION

3.1. ADOH in Cyclohexane. We start our analysis by presenting simulation results for ADOH in C_6H_{12} , i.e., the same system studied experimentally in ref 8. In this experiment, results from SAXS and NMR suggested the onset of micelle formation, with a CMC of approximately 100 mM and an average radius estimated between 1.7 and 2.5 nm. As the contour length of ADOH is ≈ 1.5 nm, the emerging scenario was that of nearly spherical micelles with all of the TEG tails buried deep inside each micelle and the adamantane hydrocarbon heads in contact with the solvent. Hence, the analogue of a conventional spherical micelle with reversed polarity of both the surfactant and the solvent.

Spherical micelles can indeed be expected on the basis of the surfactant packing parameter⁴⁰

$$N_s = \frac{V_t}{A_c l_t} \quad (5)$$

where V_t and l_t are the tail volume and length, respectively, and A_c is the contact area between the head group and the tail. In the case of ADOH $l_t = 0.93 - 1.25$ nm, $V_t \approx 0.603$ nm³ and $A_c \approx 1.55$ nm², as obtained by approximating the head group to a sphere and assuming the contact area as half of the sphere surface. This leads to $N_s = 0.312 - 0.421$, consistent with a surfactant forming spherical or cylindrical aggregates. We remark, however, that this argument assumes a tight packing in a straight conformation of the TEG tails into the core of the micelle, which contradicts the characteristic high flexibility associated with the chemical structure of the tail.

We first consider all-atom simulations to have full control over the driving forces at the microscopic level. The simulations were run at 200 mM, a concentration significantly higher than the putative experimental CMC at which an increase of the SAXS intensity was observed (≈ 100 mM).

Figure 2A shows a snapshot of the final configuration after 450 ns, and no clear sign of any sort of aggregation is visible. Clearly, this may be an issue of the atomistic simulation time scale. Indeed, even in conventional surfactants, although early aggregation already occurs in the first few nanoseconds of simulation, the time scales for the stabilization of micelles usually extend to the microseconds regime and can be most suitably probed by coarse-grained models, such as hPF-MD. The absence of stable aggregates is however confirmed by hPF-MD, as depicted by the corresponding snapshot of Figure 2B obtained after 1800 ns. Zooming in on the all-atom snapshot of Figure 2A, it is possible to see a seven-molecule aggregate, two dimers kept together by tail-tail interactions of the hydroxyl groups, and two free monomers (Figure 3A). This represents a typical transient molecular cluster that is frequently observed

Table 2. Simulation Setup

concentration (mM)	method	solvent	ADOH molecules	solvent molecules	box size (nm)	time (ns)
1	hPF-MD	H ₂ O	13	182 801	28	100
2	hPF-MD	H ₂ O	26	182 704	28	100
5	hPF-MD	H ₂ O	66	182 412	28	100
10	hPF-MD	H ₂ O	132	181 927	28	100
15	hPF-MD	H ₂ O	198	181 441	28	100
50	hPF-MD	H ₂ O	661	178 041	28	100
50	all-atom ^a	H ₂ O	661	712 490	28	50
100	hPF-MD	H ₂ O	1322	173 184	28	100
200	hPF-MD	H ₂ O	2644	163 469	28	100
200	hPF-MD	C ₆ H ₁₂	330	13 670	14	1800
200	all-atom ^a	C ₆ H ₁₂	330	11 671	14	150
200	all-atom	C ₆ H ₁₂	330	11 079	14	450

^aModel with only an effective charge in the terminal hydroxyl group of the surfactant tail.

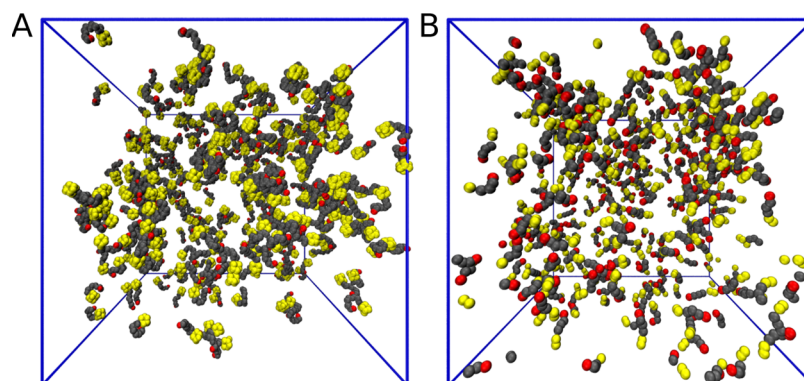


Figure 2. Final snapshots from (A) all-atom after 450 ns and (B) hPF-MD after 1800 ns simulations of 200 mM ADOH in C₆H₁₂. In both cases, the box size is 14 nm. Solvent molecules have been removed for clarity.

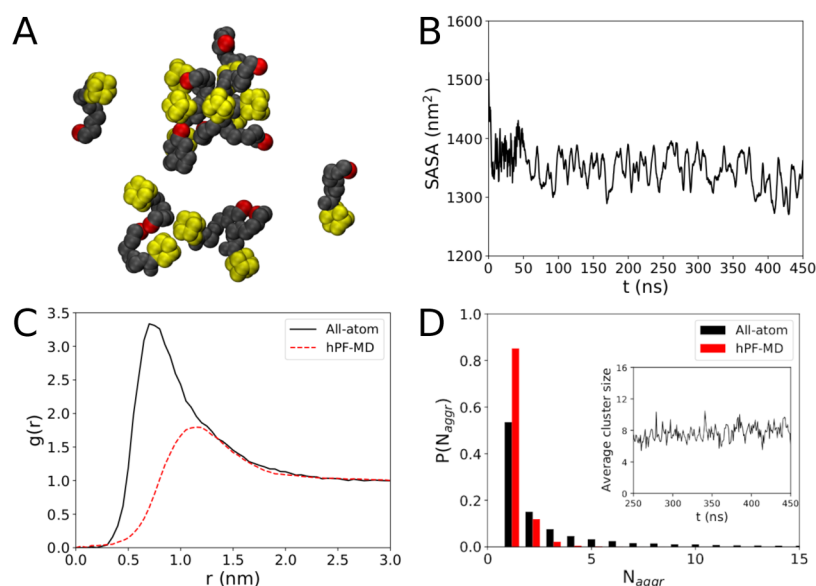


Figure 3. (A) Zoomed-in picture from the last frame of the all-atom simulation. (B) All-atom solvent-accessible surface area. (C) ADOH–ADOH radial distribution function $g(r)$ from both all-atom and hPF-MD simulations. (D) Cluster size distribution of both all-atom and hPF-MD simulations. The inset depicts the average cluster size as a function of time.

during the simulation characterized by an irregular shape and a very short lifetime in the 10^1 – 10^2 ps range. The absence of stable micelles at this concentration is confirmed by the practically flat time profile of the solvent-accessible surface area (SASA) obtained from all-atom simulations (Figure 3B),

indicating the absence of a core-collapse. The dynamical behavior of the system (see the movie provided in the SI) clearly indicates the presence of fast forming/disrupting dimers, trimers, and higher-order multimers. Nonetheless, aggregation does not seem to result in the formation of a

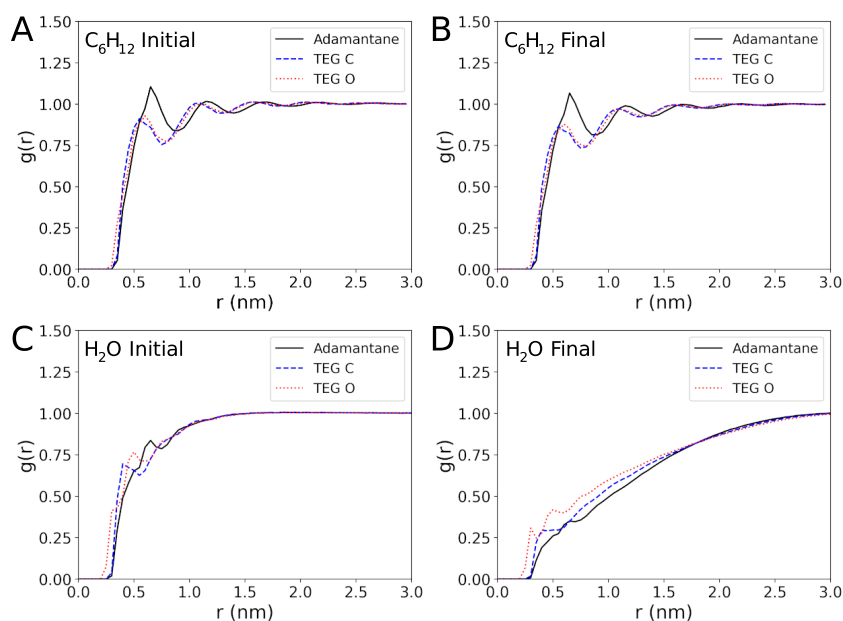


Figure 4. RDF between the solvent and the adamantane head (solid black line), TEG carbons (dashed blue line), and TEG oxygens (dotted red line) at the start and end of the simulation for both C_6H_{12} (A, B) and water (C, D).

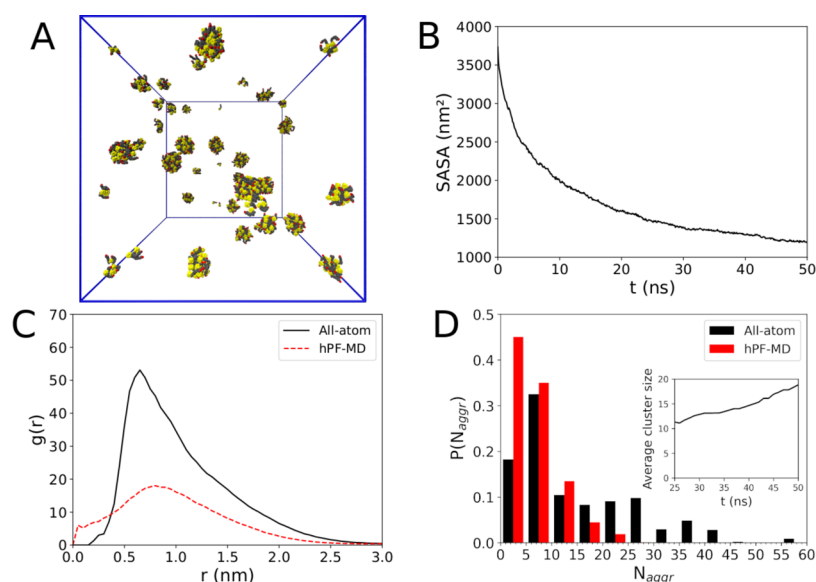


Figure 5. (A) Snapshot of a 50 mM ADOH solution in water after 50 ns of all-atom MD simulations. Water molecules have been removed for clarity. (B) All-atom solvent-accessible surface area as a function of time. (C) ADOH-ADOH radial distribution function. (D) Cluster size distribution. The inset shows the average cluster size as a function of the simulation time.

typical core, ADOH diffusion appears dominated by the monomeric phase, and the nonpolar solvent does not show any preferential affinity for either the head or the tail group. In particular, the first peak of the radial distribution function (RDF) of C_6H_{12} against the adamantane head or the TEG tail atoms is found for both cases at ~ 0.6 nm, while the profile shows the characteristic modulations typical of a good solvent (Figure 4A,B). Moreover, the RDF plot does not change over time, indicating the absence of progressive aggregation during the simulation. The all-atom ADOH-ADOH center of mass RDF reported in Figure 3C shows a broad peak at ≈ 0.75 nm and tends to reach unity at a distance of $r \approx 2$ nm, which is an indication of the presence of uncorrelated disorder beyond this range. Also shown in Figure 3C is the RDF from hPF-MD

calculation that provides a consistent picture although with a peak at a slightly larger value, indicating the tendency for the ADOH molecules to settle at this distance on a longer time scale.

The absence of well-defined aggregates for ADOH in C_6H_{12} is finally confirmed by the cluster size distribution (Figure 3D), which exhibits an exponential decay with cluster size N_{aggr} . The average cluster size remains constant during the simulation around a value of ≈ 7 , indicating that a steady state has been reached. This is further corroborated by hPF-MD simulations that do not show any formation of stable micelles even after 1800 ns (see Figure 2B) and that show the same exponential decay found for the all-atom case in the aggregation number analysis.

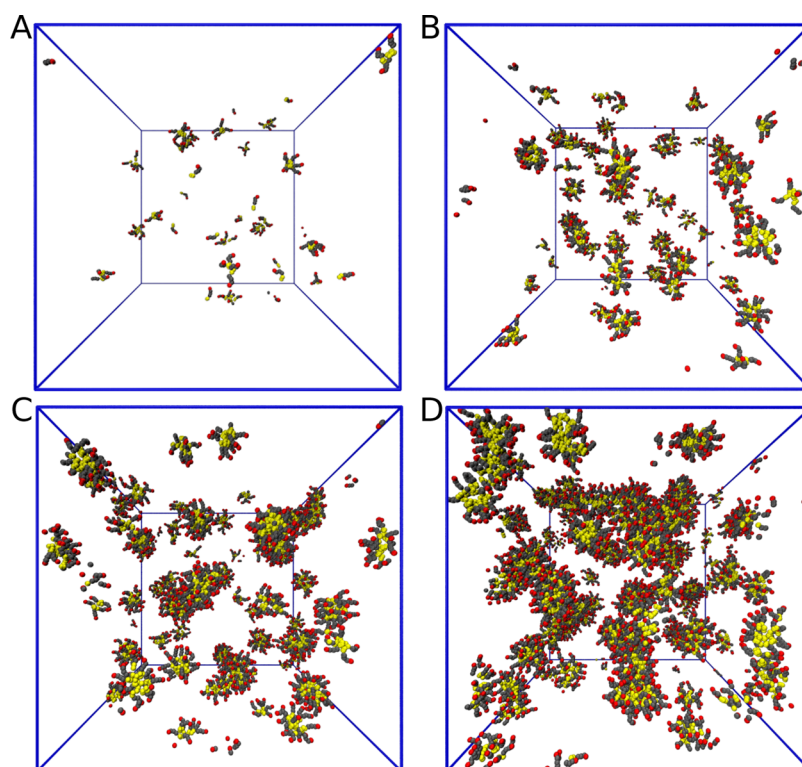


Figure 6. Hybrid particle-field snapshots of micelles formed after 100 ns in a 28 nm cubic box at different concentrations in water: (A) 10 mM, (B) 50 mM, (C) 100 mM, and (D) 200 mM.

3.2. ADOH in Water. To better understand the physics of ADOH in solution, it proves interesting to investigate the self-assembly of ADOH in water, a case that unfortunately was not covered in the experiment of ref 8. Figure 5A depicts the aggregation state for a 50 mM concentration of ADOH in water after only 50 ns of all-atom MD simulations. Even a very short simulation time window is sufficient to report evidence that ADOH self-assembles in regular spherical micelles, which is in agreement with the predictions given by its packing parameter of 0.312 and its simple molecular structure (Figure 1). The bulky hydrophobic adamantane heads of the amphiphilic molecule promote fast aggregation to minimize the contact with water, grouping together into a well recognizable hydrophobic core, while the hydroxyl groups of the TEG tails stick out into the solvent. This is also well depicted by the time evolution of the RDF profile between the ADOH moieties and the solvent (Figure 4C,D). In particular, at the end of the simulation, RDF profiles reach bulk values at much longer distances than in C_6H_{12} , a consequence of the micellar collapse that screens ADOH moieties from the solvent. There is also a clear differentiation between the RDF profiles of TEG oxygens and adamantane, indicating the expected clear preference of the solvent for the former. The opposite behavior instead does not occur in C_6H_{12} .

The formation of micelles at this concentration is confirmed by the analysis of the SASA that, unlike in C_6H_{12} , steadily decreases and levels off toward a stable value after 50 ns of MD simulations (Figure 5B). This is further supported by the ADOH–ADOH center of mass RDF reported in Figure 5C. A very broad peak at ≈ 0.75 nm indicates the smallest ADOH–ADOH distance in a dimer (see Figure 5A), while a slow decaying signal that asymptotically reaches unity at 3 nm is indicative of the several additional characteristic ADOH–

ADOH distances present in the micelle, all consistent signs of the presence of stable aggregates. The cluster size distribution analysis for the micelles (Figure 5D; here, the bin size is five units) corroborates this picture with the visible presence of a multivalued distribution and a relatively large polydispersity in micelle size, which is mainly due to the relatively short simulation times. In fact, the plot of the average cluster size as a function of time is characterized by a gradual increase in the value, indicating that the final equilibrium state is not reached.

In any case, the all-atom results are sufficient to indicate that the simulated system is well above the critical micelle concentration (CMC). To obtain a rough estimate of the CMC of ADOH in water, we repeated simulations of ADOH at progressively lower concentrations using a hPF-MD approach. Thanks to the cheaper potentials and the intrinsically accelerated dynamics, hPF-MD yields a better convergence of the aggregation state of ADOH even at much lower concentrations than 50 mM.

The hPF-MD model was first validated against reference all-atom data by running simulations at 50 mM. Figure 6 presents snapshots of the final configurations obtained after 100 ns of hPF-MD simulations at 10, 50, 100, and 200 mM concentrations. These snapshots provide clear indications of aggregation, also supported by the corresponding ADOH–ADOH RDF (not shown), all exhibiting a peak localized at 0.75 nm and a similar long-range decay (see Figure 5C). Note that the discrepancies on the height of the peak and higher distribution values at short range are a typical feature of hPF models and must be attributed to the soft nature of the hPF potential.

From the morphological viewpoint, the size of the aggregates increases with solute concentration and at 200 mM, micelles start fusing together to form tubular structures. This is

consistent with the concentration-dependent smooth transition from spherical to tubular micelles that is commonly observed in more conventional amphiphilic surfactants and can be ascribed to the reaching of a critical packing of the hydrophobic moieties, above which they can no longer be accommodated into a compact spherical volume.^{29,41,42}

The absence of significant aggregated units at 10 mM suggests that, in water, the CMC for ADOH is between 10 and 50 mM. We repeated additional hPF-MD simulations at progressively higher ADOH dilutions (1, 2, 5, and 15 mM). By performing a linear fit of the concentration dependence of the free monomer fraction on the surfactant concentration at smaller and higher values than the CMC and determining their intersection point, we produce the best estimate for the CMC \approx 13.5 mM (Figure 7). Here, we notice that the number of

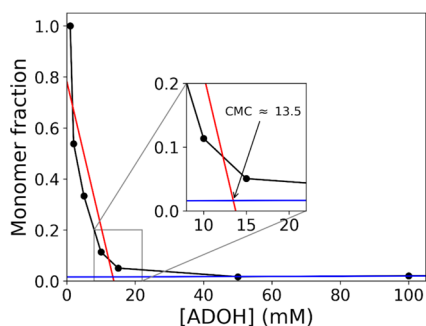


Figure 7. CMC determination by the linear fitting of the two distinct regions present in the monomer fraction vs surfactant concentration plot.

surfactant molecules present in the lowest concentration simulation is quite small, hence the value of the first point in Figure 7 could be lower if we accounted for possible finite-size errors. However, even changing the monomer fraction in the range 0.9–0.7, the error in the CMC is only \sim 1–4%.

3.3. Reconciling with the Experiment. The interpretation of the experimental results of ADOH in C_6H_{12} in terms of formation of well-defined micelles above a CMC \approx 100 mM⁸ and the numerical simulations that found no evidence of a stable micellization process are in apparent contradiction.

In fact, formation of aggregates was originally suggested on the basis of two pieces of experimental evidence: (i) a significantly lower diffusion constant for ADOH compared to that of the pure solvent and (ii) a marked change in the SAXS intensity signal for concentrations above 100 mM.

Diffusion Coefficient. Diffusion coefficients for C_6H_{12} , water, and ADOH in the two solvents were estimated from the slope of the mean square deviation (MSD), $\sigma^2(t)$, calculated for all-atom simulations according to the Einstein diffusion equation, $\sigma^2(t) = 6Dt + A$, and compared with experimental results obtained from ¹H two-dimensional diffusion-ordered spectroscopy (2D-DOSY) NMR measurements. Table 3 reports the comparison between experimental diffusion coefficients (first column) and the corresponding all-atom estimates (third column) and provides evidence of a reasonably good agreement. The results of the second column will be discussed further below. On this basis, we now argue that the drop observed in the experiment might be due to other reasons and not related to the micellization process.

SAXS Spectrum. Figure 8 shows the experimental SAXS data for a 200 mM concentration of ADOH in C_6H_{12} taken

Table 3. Diffusion Coefficients (10^{-5} cm²/s) Calculated from Mean Square Displacement Analysis of the All-Atom Simulations Compared with Experimental Results^a

	experimental	all-atom w/ partial charges	all-atom w/o partial charges
C_6H_{12}	1.48 ⁸	1.50 ± 0.02	1.38 ± 0.02
ADOH	0.47 ⁸	0.63 ± 0.03	0.48 ± 0.01
H_2O	2.30 ⁴³	3.90 ± 0.01	
ADOH		0.35 ± 0.02	

^aFirst column, experimental results (250 mM); second column, all-atom simulations without partial charges; and third column, all-atom simulations with partial charges. The concentrations are 200 mM for simulations in C_6H_{12} and 50 mM for H_2O .

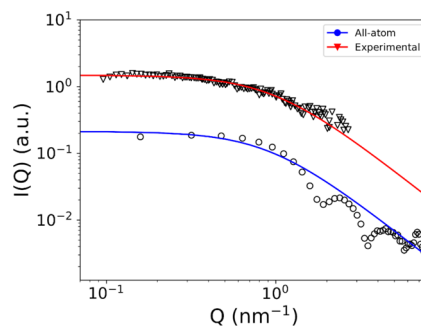


Figure 8. SAXS data extracted from ref 8 (triangles) compared to the one calculated by a Fourier transform of the RDF from our all-atom simulation at 200 mM ADOH in C_6H_{12} (circles). The red and blue lines are the corresponding fits to eq 6.

from ref 8. Interestingly, the line is not characterized by a marked drop of the intensity as expected for regular spherical objects of a well-defined radius. Rather, at a higher scattering vector Q , it decays slowly and without showing any particular feature, a behavior compatible with the presence of irregular objects with no clear size. This is in very good qualitative agreement with our simulations, which show the absence of a well-defined organization of the surfactant. The molecular RDF, in particular, is characterized by a simple profile with a short-range peak and a fast decay (Figure 3C). Assuming a similar situation in the experiment, with an exponentially decaying RDF, the spectral SAXS line would then have the following form

$$I(Q) = \frac{A}{1 + \xi^2 Q^2} \quad (6)$$

where ξ is the Ornstein–Zernike correlation length.⁴⁴ As can be observed in Figure 8, such line shape fits well the experimental data. For comparison, we report the predicted SAXS spectrum obtained by Fourier transform of the RDF from the all-atom simulation, as well as its fitting by eq 6. Like for the diffusion coefficient, the agreement with the fit on the SAXS measurements is an indication that our computational model is well in line with the experimental findings.

Driving Forces of ADOH Interactions in C_6H_{12} . The standard understanding of micelle formation is based on the hydrophobic effect, which is an entropy-driven phenomenon. By contrast, in C_6H_{12} , the formation of ADOH clusters is likely to be penalized entropically due to the necessary confinement of TEG tails in the micellar core. Rather, ADOH aggregates might be stabilized by the enthalpy gain associated with the electrostatic interactions occurring among the polar TEG

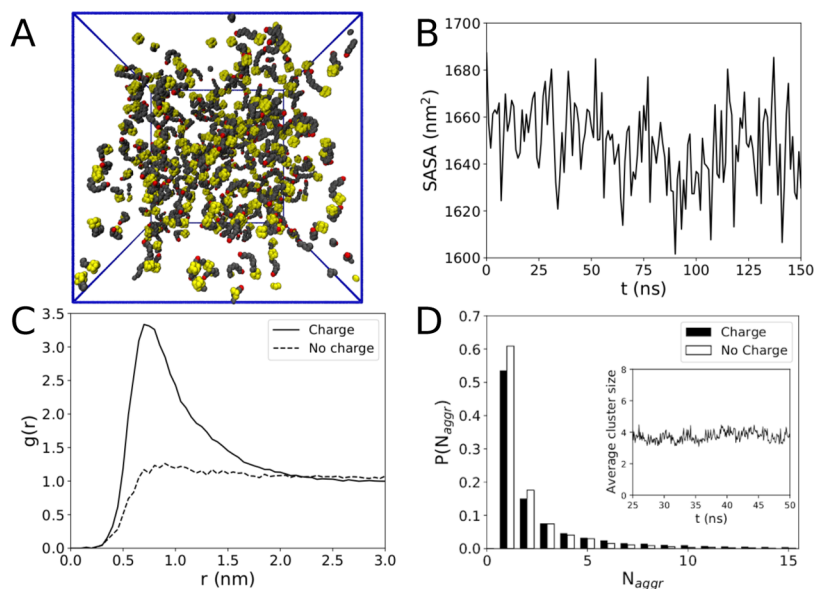


Figure 9. (A) All-atom simulation of 200 mM ADOH in C_6H_{12} without partial charges. (B) SASA as a function of simulation time. (C) Comparison of RDF with and without partial charges. (D) Same as in (C) for the cluster size distribution.

segments when two TEG tails rest at a close distance. If so, the lower diffusion coefficient for ADOH would be explained in terms of molecular crowding, where the pathway of a freely diffusing ADOH is hindered by the interaction with other ADOH molecules. This would have the effect of increasing the local viscosity of the medium, thus reducing diffusion even in the absence of a stable aggregate formation.

To verify this hypothesis, we ran additional all-atom simulations of ADOH in both water and C_6H_{12} where all partial charges on the TEG segment of the amphiphile were set to zero and replaced by an effective dipole in the final hydroxyl group mimicking the total dipole of the tail. These artificial systems keep a coarse representation of the polarity of the TEG tail while at the same time removing the quadrupolar charge distributions characteristic of the glycol ether moieties. The presence of a finite dipole on the terminal OH also ensures a correct representation of the terminal H-bonding group, which was hypothesized to be crucial for ADOH aggregation in C_6H_{12} .

Simulations in water, discussed in Section 3.2, resulted in a faster formation of micelles compared to what was observed for the physical model (not shown). In C_6H_{12} , the absence of quadrupolar charges on the TEG segment reduces even further the aggregation of ADOH, resulting in a net 30% increase of its diffusion coefficient (see the second column in Table 3).

The final snapshot of this system in C_6H_{12} after 150 ns is shown in Figure 9A, while the SASA is reported in Figure 9B. Clear differences in the aggregation behavior are evident by inspecting the RDF between ADOH molecules (Figure 9C). In the absence of partial charges on the TEG segment, the RDF does not show a clear first-neighbor peak. On the contrary, the RDF reaches unity immediately at $r = 1$ nm, which implies that each molecule is spatially uncorrelated from one another and that the distribution of surfactant in the sample is practically uniform. The distribution of the aggregation number (Figure 9D) shows a marked difference with the distribution more skewed toward the monomer peak rather than larger aggregates and an average cluster size of N_{aggr}

$= 4$ significantly smaller than the original model with all of the partial charges (compare with the inset of Figure 3D).

Formation of hydrogen bonding between the hydroxyl groups at the tails of ADOH was also putatively indicated as a possible driving force for ADOH aggregation in C_6H_{12} . Figure 10 reports the number of hydrogen bonds per ADOH

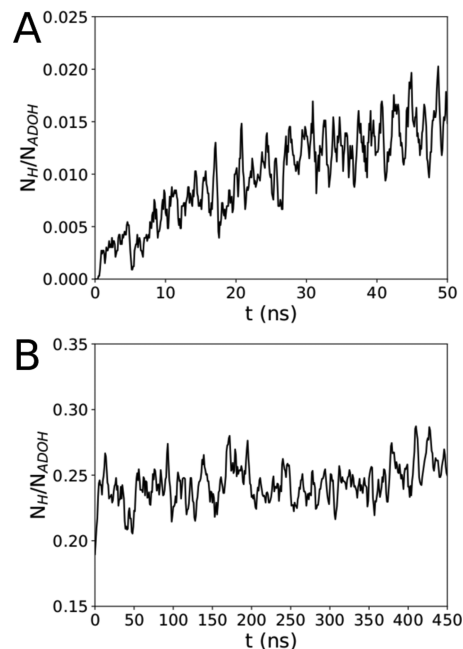


Figure 10. Number of hydrogen bonds between ADOH molecules as a function of time in all-atom simulations in (A) water and (B) C_6H_{12} .

molecule (N_H/N_{ADOH}) as a function of time in water and C_6H_{12} . As expected, the number of H-bonds between ADOH in water is marginal, as the strongly hydrophilic groups prefer to interact with the solvent (see Figure 10A). However, in C_6H_{12} , a significant fraction of ADOH is involved in H-bonds, with a very stable average of ≈ 0.25 H-bonds per molecule, as shown in Figure 10B. This number is anyway much smaller

than the theoretical number of H-bonds expected in the sample if clustering between ADOH molecules was determined by H-bonding. In fact, assuming that all clustered ADOH molecules would be involved in at least a single H-bond and considering the average cluster size (see the inset in Figure 3D), one would expect a value of ~ 0.87 H-bonds per molecule, which is almost three times the one observed. This finding confirms that while H-bonds between ADOH tails can contribute to the binding interactions, they themselves are not strong enough to constitute a significant driving force for ADOH aggregation.

Overall, simulations of the artificial system without TEG charges confirm that cohesion of ADOH in C_6H_{12} is an enthalpy-dominated phenomenon mainly due to quadrupole–quadrupole interactions between the TEG polar regions. This is qualitatively different from the situation in water, where the collapse of the surfactant is determined by the entropy and where the same qualitative effect could be obtained by lumping all partial charges of TEG into an effective dipole on the hydroxyl group at the end of the tail. Our simulations in C_6H_{12} indicate the presence of small, labile ADOH clusters rapidly forming and dissolving in the sample. The presence of an appreciable density dishomogeneity in the absence of true stable aggregates is indicative of a mixture at supercritical conditions, confirmed by the shape of the SAXS profile, in qualitative agreement with those observed in other supercritical mixtures, for example, water/acetone. ⁴⁵

4. CONCLUSIONS

We performed a detailed computational analysis of the self-assembly process of ADOH surfactants composed of a hydrophobic adamantane head and a TEG tail terminating with an OH hydroxyl group. We have studied the mechanism driving the formation of aggregates in C_6H_{12} by comparing their sizes, distributions, interactions, as well as their diffusion coefficients with their experimental counterparts. ⁸ In addition, we have also studied the same system in water providing a qualitative prediction for all of the above quantities that could be experimentally tested. By a detailed analysis of the results under different concentrations, we have also been able to estimate a value of 13.5 mM for the CMC in water.

Our parallel analysis in water and C_6H_{12} has allowed us to underpin the different forces driving the self-assembly in the two solvents. In water, the conventional hydrophobic effect plays a major role in promoting the aggregation of the hydrophobic heads that are buried inside the micelles to avoid direct contact with water molecules. In C_6H_{12} , an analogous lipophobic effect does not occur, and formation of well-defined micelles with an inverted structure was not observed. The lack of such an effect may be attributed to concomitant factors, including the fact that TEG chains are not as lipophobic as adamantane is hydrophobic and that the conformational frustration of the flexible TEG moieties is insufficiently balanced by the solvent entropy release associated with the collapse of an aggregate.

Our investigation highlighted the fact that the aggregation of ADOH into low-weight oligomers is sufficient to explain the decrease of diffusion coefficient experimentally observed, as well as the previously reported SAXS data. Formation of these oligomers is determined by short-range attraction of the electrostatic quadrupoles distributed over the TEG segment. By contrast, in water, these interactions are favored by the low dielectric screening due to the weakly polarizable solvent.

However promising, ADOH in C_6H_{12} appears to linger in a supercritical phase without a clear collapse into well-defined self-assembled aggregates. Our study points to multiple possible routes that could produce significant steps toward such a goal. First, there is the need of decreasing the entropy of the free TEG chain to reduce the entropy loss upon confinement of the polar regions in the micellar core. This could be achieved by narrowing the accessible conformational space of the TEG chain already in the monomer, for example, by adding a second TEG unit to the ADOH structure. Additionally, it might be possible to chemically modify the TEG part or to use other polymers having an even stronger polar character. While these two options aim for raising the critical temperature of the systems, it is worth mentioning the even simpler idea of studying ADOH dissolved in low-freezing-point solvents. This option should be considered in particular thinking of other thermodynamic regimes (high pressure, low temperature) that could be found in extraterrestrial environments. Synthetic effort in this direction may soon lead to the determination of surfactants having the ability of inverting their aggregation structure in solvents of radically different polarities.

■ ASSOCIATED CONTENT

Supporting Information

The Supporting Information is available free of charge at <https://pubs.acs.org/doi/10.1021/acs.jpbc.0c04842>.

We provide a short movie for the all-atom simulation of ADOH in C_6H_{12} to show the fast aggregation/disaggregation process (MPG)

■ AUTHOR INFORMATION

Corresponding Author

Achille Giacometti – Dipartimento di Scienze Molecolari e Nanosistemi, Università Ca' Foscari di Venezia, Campus Scientifico, 30170 Venezia Mestre, Italy; European Centre for Living Technology (ECLT) Ca' Bottacin, 30123 Venice, Italy; orcid.org/0000-0002-1245-9842; Phone: +39 041 234 8685; Email: achille.giacometti@unive.it

Authors

Manuel Carrer – Department of Chemistry and Hylleraas Centre for Quantum Molecular Sciences, University of Oslo, 0315 Oslo, Norway

Tatjana Škrbić – Department of Physics and Institute for Fundamental Science, University of Oregon, Eugene, Oregon 97403, United States; Dipartimento di Scienze Molecolari e Nanosistemi, Università Ca' Foscari di Venezia, Campus Scientifico, 30170 Venezia Mestre, Italy

Sigbjørn Løland Bore – Department of Chemistry and Hylleraas Centre for Quantum Molecular Sciences, University of Oslo, 0315 Oslo, Norway; orcid.org/0000-0002-8620-4885

Giuseppe Milano – Department of Organic Materials Science, Yamagata University, Yonezawa 992-8510, Yamagata-ken, Japan; Dipartimento di Chimica e Biologia, Università di Salerno, 84084 Fisciano, Italy

Michele Cascella – Department of Chemistry and Hylleraas Centre for Quantum Molecular Sciences, University of Oslo, 0315 Oslo, Norway; orcid.org/0000-0003-2266-5399

Complete contact information is available at:

<https://pubs.acs.org/doi/10.1021/acs.jpbc.0c04842>

Notes

The authors declare no competing financial interest.

ACKNOWLEDGMENTS

We are indebted to Paul Dupire and Emanuele Petretto for their help at the initial stage of the project and to the authors of ref 8 for useful discussions. The authors would also like to thank Reidar Lund for his precious help with the interpretation of SAXS data. This work was supported by the Research Council of Norway (RCN) through the CoE Hylleraas Centre for Quantum Molecular Sciences (Grant number 262695), by the Norwegian Supercomputing Program (NOTUR) (Grant number NN4654K), by MIUR PRIN-COFIN2017 Soft Adaptive Networks grant 2017Z55KCW, by Marie Curie Sklodowska-Curie Fellowship No. 894784 EMPHABIOSYS, and by a Knight Chair to Prof. Jayanth Banavar at University of Oregon (T.S.). The use of the SCSCF multiprocessor cluster at the Università Ca' Foscari Venezia is gratefully acknowledged. The authors would like to acknowledge networking support by the COST Action CA17139.

REFERENCES

- (1) Tanford, C. *The Hydrophobic Effect: Formation of Micelles and Biological Membranes*; John Wiley & Sons: New York, 1973.
- (2) Israelachvili, J. N. *Intermolecular and Surface Forces*, 3rd ed.; Academic Press: Boston, 2011.
- (3) Sandström, H.; Rahm, M. Can Polarity-Inverted Membranes Self-Assemble on Titan. *Sci. Adv.* **2020**, *6*, No. eaax0272.
- (4) Pace, C. N.; Trevino, S.; Prabhakaran, E.; Scholtz, J. M. Protein Structure, Stability and Solubility in Water and Other Solvents. *Philos. Trans. R. Soc., B* **2004**, *359*, 1225–1235.
- (5) Hayashi, T.; Yasuda, S.; Škrbić, T.; Giacometti, A.; Kinoshita, M. Unraveling Protein Folding Mechanism by Analyzing the Hierarchy of Models with Increasing Level of Detail. *J. Chem. Phys.* **2017**, *147*, No. 125102.
- (6) Hayashi, T.; Inoue, M.; Yasuda, S.; Petretto, E.; Škrbić, T.; Giacometti, A.; Kinoshita, M. Universal Effects of Solvent Species on the Stabilized Structure of a Protein. *J. Chem. Phys.* **2018**, *149*, No. 045105.
- (7) Hamlin, T. A.; Poater, J.; Fonseca Guerra, C.; Bickelhaupt, F. M. B-DNA Model Systems in Non-Terran Bio-Solvents: Implications for Structure, Stability and Replication. *Phys. Chem. Chem. Phys.* **2017**, *19*, 16969–16978.
- (8) Facchin, M.; Scarso, A.; Selva, M.; Perosa, A.; Riello, P. Towards Life in Hydrocarbons: Aggregation behaviour of “Reverse” Surfactants in Cyclohexane. *RSC Adv.* **2017**, *7*, 15337–15341.
- (9) Voth, G. A. *Coarse-Graining of Condensed Phase and Biomolecular Systems*; CRC Press: Boca Raton, 2008.
- (10) Marrink, S. J.; Tieleman, D. P. Perspective on the Martini model. *Chem. Soc. Rev.* **2013**, *42*, 6801–6822.
- (11) Milano, G.; Kawakatsu, T.; De Nicola, A. A Hybrid Particle-Field Molecular Dynamics Approach: A Route toward Efficient Coarse-Grained Models for Biomembranes. *Phys. Biol.* **2013**, *10*, No. 045007.
- (12) Soares, T. A.; Vanni, S.; Milano, G.; Cascella, M. Toward Chemically Resolved Computer Simulations of Dynamics and Remodeling of Biological Membranes. *J. Phys. Chem. Lett.* **2017**, *8*, 3586–3594.
- (13) Cascella, M.; Vanni, S. *Chemical Modelling: Applications and Theory*; Springborg, M.; Joswig, J.-O., Eds.; Royal Society of Chemistry: London, 2015; Vol. 12; Chapter 1, pp 1–52.
- (14) Marrink, S. J.; Corradi, V.; Souza, P. C.; Ingólfsson, H. I.; Tieleman, D. P.; Sansom, M. S. Computational Modeling of Realistic Cell Membranes. *Chem. Rev.* **2019**, *119*, 6184–6226.
- (15) De Nicola, A.; Kawakatsu, T.; Müller-Plathe, F.; Milano, G. Fast Relaxation of Coarse-Grained Models of Polymer Interphases by Hybrid Particle-Field Molecular Dynamics: Polystyrene-Silica Nanocomposites As an Example. *Eur. Phys. J.: Spec. Top.* **2016**, *225*, 1817–1841.
- (16) Zhao, Y.; Byshkin, M.; Cong, Y.; Kawakatsu, T.; Guadagno, L.; De Nicola, A.; Yu, N.; Milano, G.; Dong, B. Self-Assembly of Carbon Nanotubes in Polymer Melts: Simulation of Structural and Electrical Behaviour by Hybrid Particle-Field Molecular Dynamics. *Nanoscale* **2016**, *8*, 15538–15552.
- (17) Munaò, G.; Pizzirusso, A.; Kalogirou, A.; De Nicola, A.; Kawakatsu, T.; Müller-Plathe, F.; Milano, G. Molecular Structure and Multi-Body Potential of Mean Force in Silica-Polystyrene Nanocomposites. *Nanoscale* **2018**, *10*, 21656–21670.
- (18) Munaò, G.; De Nicola, A.; Müller-Plathe, F.; Kawakatsu, T.; Kalogirou, A.; Milano, G. Influence of Polymer Bidispersity on the Effective Particle-Particle Interactions in Polymer Nanocomposites. *Macromolecules* **2019**, *52*, 8826–8839.
- (19) De Nicola, A.; Zhao, Y.; Kawakatsu, T.; Roccatano, D.; Milano, G. Validation of a Hybrid MD-SCF Coarse-Grained Model for DPPC in Non-Lamellar Phases. *Theor. Chem. Acc.* **2012**, *131*, 1167.
- (20) Ledum, M.; Bore, S. L.; Cascella, M. Automated Determination of Hybrid Particle-Field Parameters by Machine Learning. *Mol. Phys.* **2020**, published online, <https://doi.org/10.1080/00268976.2020.1785571>.
- (21) De Nicola, A.; Zhao, Y.; Kawakatsu, T.; Roccatano, D.; Milano, G. Hybrid Particle-Field Coarse-Grained Models for Biological Phospholipids. *J. Chem. Theory Comput.* **2011**, *7*, 2947–2962.
- (22) Bore, S. L.; Kolli, H. B.; De Nicola, A.; Byshkin, M.; Kawakatsu, T.; Milano, G.; Cascella, M. Hybrid Particle-Field Molecular Dynamics under Constant Pressure. *J. Chem. Phys.* **2020**, *152*, No. 184908.
- (23) Bore, S. L.; Milano, G.; Cascella, M. Hybrid Particle-Field Model for Conformational Dynamics of Peptide Chains. *J. Chem. Theory Comput.* **2018**, *14*, 1120–1130.
- (24) Zhu, Y.-L.; Lu, Z.-Y.; Milano, G.; Shi, A.-C.; Sun, Z.-Y. Hybrid Particle-Field Molecular Dynamics Simulation for Polyelectrolyte Systems. *Phys. Chem. Chem. Phys.* **2016**, *18*, 9799–9808.
- (25) Kolli, H. B.; De Nicola, A.; Bore, S. L.; Schäfer, K.; Diezemann, G.; Gauss, J.; Kawakatsu, T.; Lu, Z.-Y.; Zhu, Y.-L.; Milano, G.; et al. Hybrid Particle-Field Molecular Dynamics Simulations of Charged Amphiphiles in an Aqueous Environment. *J. Chem. Theory Comput.* **2018**, *14*, 4928–4937.
- (26) Bore, S. L.; Kolli, H. B.; Kawakatsu, T.; Milano, G.; Cascella, M. Mesoscale Electrostatics Driving Particle Dynamics in Nonhomogeneous Dielectrics. *J. Chem. Theory Comput.* **2019**, *15*, 2033–2041.
- (27) De Nicola, A.; Soares, T. A.; Santos, D. E.; Bore, S. L.; Sevinck, G. A.; Cascella, M.; Milano, G. Aggregation of Lipid A Variants: A Hybrid Particle-Field Model. *Biochim. Biophys. Acta, Gen. Subj.* **2020**, 129570.
- (28) Schäfer, K.; Kolli, H. B.; Christensen, M. K.; Bore, S. L.; Diezemann, G.; Gauss, J.; Milano, G.; Lund, R.; Cascella, M. Supramolecular Packing Drives Morphological Transition of Charged Surfactant Micelles. *Angew. Chem., Int. Ed.* **2020**, No. 2004522.
- (29) Pizzirusso, A.; De Nicola, A.; Sevinck, G. J. A.; Correa, A.; Cascella, M.; Kawakatsu, T.; Rocco, M.; Zhao, Y.; Celino, M.; Milano, G. Biomembrane Solubilization Mechanism by Triton X-100: A Computational Study of the Three Stage Model. *Phys. Chem. Chem. Phys.* **2017**, *19*, 29780–29794.
- (30) Robertson, M. J.; Tirado-Rives, J.; Jorgensen, W. L. Improved Peptide and Protein Torsional Energetics with the OPLS-AA Force Field. *J. Chem. Theory Comput.* **2015**, *11*, 3499–3509.
- (31) Bussi, G.; Donadio, D.; Parrinello, M. Canonical Sampling through Velocity Rescaling. *J. Chem. Phys.* **2007**, *126*, No. 014101.
- (32) Parrinello, M.; Rahman, A. Polymorphic Transitions in Single Crystals: A New Molecular Dynamics Method. *J. Appl. Phys.* **1981**, *52*, 7182–7190.
- (33) Hess, B.; Bekker, H.; Berendsen, H. J. C.; Fraaije, J. G. E. M. LINCS: A Linear Constraint Solver for Molecular Simulations. *J. Comput. Chem.* **1997**, *18*, 1463–1472.

- (34) Jorgensen, W. L.; Chandrasekhar, J.; Madura, J. D.; Impey, R. W.; Klein, M. L. Comparison of Simple Potential Functions for Simulating Liquid Water. *J. Chem. Phys.* **1983**, *79*, 926–935.
- (35) Jorgensen, W. L.; Maxwell, D. S.; Tirado-Rives, J. Development and Testing of the OPLS All-Atom Force Field on Conformational Energetics and Properties of Organic Liquids. *J. Am. Chem. Soc.* **1996**, *118*, 11225–11236.
- (36) Abraham, M. J.; Murtola, T.; Schulz, R.; Páll, S.; Smith, J. C.; Hess, B.; Lindahl, E. GROMACS: High Performance Molecular Simulations through Multi-Level Parallelism from Laptops to Supercomputers. *SoftwareX* **2015**, *1*, 19–25.
- (37) Milano, G.; Kawakatsu, T. Hybrid Particle-Field Molecular Dynamics Simulations for Dense Polymer Systems. *J. Chem. Phys.* **2009**, *130*, No. 214106.
- (38) Zhao, Y.; De Nicola, A.; Kawakatsu, T.; Milano, G. Hybrid Particle-Field Molecular Dynamics Simulations: Parallelization and Benchmarks. *J. Comput. Chem.* **2012**, *33*, 868–880.
- (39) Andersen, H. C. Molecular Dynamics Simulations at Constant Pressure and/or Temperature. *J. Chem. Phys.* **1980**, *72*, 2384–2393.
- (40) Israelachvili, J. N.; Mitchell, D. J.; Ninham, B. W. Theory of Self-Assembly of Hydrocarbon Amphiphiles into Micelles and Bilayers. *J. Chem. Soc., Faraday Trans. 2* **1976**, *72*, 1525–1568.
- (41) Velinova, M.; Sengupta, D.; Tadjer, A. V.; Marrink, S.-J. Sphere-to-Rod Transitions of Nonionic Surfactant Micelles in Aqueous Solution Modeled by Molecular Dynamics Simulations. *Langmuir* **2011**, *27*, 14071–14077.
- (42) De Nicola, A.; Kawakatsu, T.; Rosano, C.; Celino, M.; Rocco, M.; Milano, G. Self-Assembly of Triton X-100 in Water Solutions: A Multiscale Simulation Study Linking Mesoscale to Atomistic Models. *J. Chem. Theory Comput.* **2015**, *11*, 4959–4971.
- (43) Holz, M.; Heil, S. R.; Sacco, A. Temperature-Dependent Self-Diffusion Coefficients of Water and Six Selected Molecular Liquids for Calibration in Accurate ¹H NMR PFG Measurements. *Phys. Chem. Chem. Phys.* **2000**, *2*, 4740–4742.
- (44) Barrat, J.-L.; Hansen, J.-P. *Basic Concepts for Simple and Complex Liquids*; Cambridge University Press: Cambridge, U.K, 2003.
- (45) Nishikawa, K.; Kasahara, Y.; Ichioka, T. Inhomogeneity of Mixing in Acetonitrile Aqueous Solution Studied by Small-Angle X-Ray Scattering. *J. Phys. Chem. B* **2002**, *106*, 693–700.